PHYSICAL REVIEW B **105**, 224101 (2022)

Strain manipulation of ferroelectric skyrmion bubbles in a freestanding $PbTiO_3$ film: A phase field simulation

Yixuan Zhang,[1] Qian Li,[2] Houbing Huang,[3,*] Jiawang Hong,[1,†] and Xueyun Wang[1,‡]
[1]School of Aerospace Engineering, Beijing Institute of Technology, Beijing 100081, China
[2]State Key Laboratory of New Ceramics and Fine Processing, School of Materials Science and Engineering, Tsinghua University, Beijing 100084, China
[3]Advanced Research Institute of Multidisciplinary Science, Beijing Institute of Technology, Beijing 100081, China

(Received 1 February 2022; revised 8 April 2022; accepted 9 May 2022; published 3 June 2022)

So far nanoscale topological polar structures have been mainly observed in ferroelectric superlattices, nanodots, and complex heterostructures, originating from the intricate interplay of built-in electric field, polarization, strain, and their gradient-related energies. However, solid substrates hinder the continuous strain manipulation of the ferroelectric topological textures. Recently, a breakthrough in fabricating freestanding films has demonstrated the possibility of continuous strain manipulation, but there has been little experimental or theoretical investigation of whether polar topological structures exist in freestanding films. Herein, by performing phase field simulation on $(PbTiO_3)_{20}/(SrTiO_3)_{10}$ freestanding bilayers, we observed the stabilized ferroelectric skyrmion bubbles in a ferroelectric layer. A thickness-dependent phase diagram indicates that the skyrmion bubbles exist when the ferroelectric layer is between eight and 30 unit cells. Meanwhile, we demonstrated that the uniaxial strain is an effective way to manipulate the skyrmion bubble in freestanding films, which not only induces consolidation and rearrangement of skyrmion bubbles, but also induces a phase transition from the topological skyrmion bubble state to a standard a_1/a_2 domain state. These results provide us guidance with a mechanical approach to control topological polar structures in freestanding films.

DOI: 10.1103/PhysRevB.105.224101

I. INTRODUCTION

Engendered by the subtle interplay among polarization, built-in electric field, strain, and related gradients, a plethora of nontrivial topological polar structures have been intensively explored over the past decade, such as flux-closure [1–4], vortex [5–8], skyrmion bubble [9–12], meron [13], and labyrinthine [14]. Novel nanostructures bring fascinating physical characteristics, such as negative capacitance [15–17], the negative electrocaloric effect [18], chirality emergence [19,20], and enhanced piezoelectricity [21], paving the way to potentially applicable devices in new conceptual information storage [22], neuromorphic computing [23], and ultrahigh-frequency devices [24–27]. However, the formation of such topological structures requires harsh energy conditions and delicate balance among different intercoupled energies, which are mostly realized and stabilized in nanodots, superlattices, heterostructures, and ferroelectric ceramics/polycrystals [28–32]. Though the lattice mismatching between the sample and substrate gives a straining effect together with strain relaxation, there is a severe lack of a continuous strain tuning method, mainly restricted by the substrate strain.

Benefits from the advanced development of thin film fabrication techniques, including ferroelectric freestanding thin films scaling down to a single unit cell (u.c.), have been realized by utilizing a sacrificial buffer layer [33,34]. Transferring such freestanding films onto a stretchable polymer leads to the possibility of continuous strain tuning, which has been successfully demonstrated experimentally with strain $\geqslant 8\%$ [35,36]. Therefore, the stabilization of the above-mentioned topological structures and possible continuous strain manipulation of these structures in freestanding ferroelectric films are questions that naturally arise. Very recently, a few pioneering works have reported the observation of topological domains in freestanding films, such as bubble domains in $PbZr_{0.2}Ti_{0.8}O_3$ (PZT) (3 nm)/$SrTiO_3$ (STO) (2 nm)/$PbZr_{0.2}Ti_{0.8}O_3$ (3 nm) freestanding films [37], and skyrmionlike nanodomains in $(PbTiO_3)_{20}/(SrTiO_3)_{10}$ freestanding bilayers [38].

Here in this paper, by performing phase field simulation, we report the observation of stable ferroelectric skyrmion bubbles in freestanding $(PbTiO_3)_{20}/(SrTiO_3)_{10}$ [$(PTO)_{20}/(STO)_{10}$] bilayers. Meanwhile, a phase diagram of the ferroelectric domains (including *a*/*c* domains, skyrmion bubbles, and flux-closure) on the different thicknesses of $PbTiO_3$ has been presented, which gives the thickness range for stabilizing the ferroelectric skyrmion bubbles. More importantly, mechanical manipulation using in-plane (IP) uniaxial strain fields is investigated in detail. Our results demonstrate a similar evolutionary behavior of the helical

---

[*] hbhuang@bit.edu.cn
[†] hongjw@bit.edu.cn
[‡] xueyun@bit.edu.cn

phase transition in ferromagnetic thin films [39,40], and provide theoretical guidance of the strain tuning of polar topological configurations.

II. PHASE FIELD METHOD

To describe ferroelectric $(\mathrm{PTO})_{20}/(\mathrm{STO})_{10}$ freestanding bilayers with skyrmion bubbles, we assume that the bilayer system was grown on the $\mathrm{SrTiO_3}$ substrate first, and then released from the substrate to conduct the research. A three-dimensional (3D) spontaneous polarization vector $\boldsymbol{P} = (P_x, P_y, P_z)$ is chosen as the order parameter. By solving time-dependent Ginzburg-Landau equations, the temporal evolution of $\boldsymbol{P}$ is obtained,

$$\frac{\partial P_{\mathrm{i}}(\boldsymbol{r},t)}{\partial t} = -L\frac{\delta F}{\delta P_{\mathrm{i}}(\boldsymbol{r},t)},\quad i = 1-3, \tag{1}$$

where $\boldsymbol{r}$ is the spatial direction vector, L is the kinetic coefficient, and t is evolutionary time. F demonstrates total free energy density, consisting of the contributions from Landau energy, gradient energy, elastic energy, and electric energy,

$$f = \iiint [f_{\mathrm{Landau}}(P_i) + f_{\mathrm{Gradient}}(P_{i,j}) + f_{\mathrm{Electric}}(P_i, E_i) + f_{\mathrm{Elastic}}(P_i, \varepsilon_{ij})]dV. \tag{2}$$

The Landau energy can be expanded into the sixth-order series polynomial form:

$$f_{\mathrm{Landau}} = a_{ij}P_iP_j + a_{ijkl}P_{\mathrm{i}}P_{\mathrm{j}}P_{\mathrm{k}}P_{\mathrm{l}} + a_{ijklmn}P_iP_jP_kP_lP_mP_n. \tag{3}$$

The gradient energy can be written as

$$f_{\mathrm{Gradient}} = \tfrac{1}{2}G_{ijkl}P_{i,j}P_{k,l}, \tag{4}$$

where G_{ijkl} denotes the gradient energy coefficient; $P_{i,j}$ denotes first-order spatial derivation of polarization vector. The electric energy density is given by

$$f_{\mathrm{Electric}} = -P_iE_i - \tfrac{1}{2}\varepsilon_0\chi_{ij}E_iE_i, \tag{5}$$

where χ_{ij} indicates the relative permittivity; ε_0 is the dielectric constant of the vacuum. Meanwhile, an open-current electric boundary condition is applied in the out of plane direction. The elastic energy is expressed in the following form,

$$f_{\mathrm{Elastic}} = \tfrac{1}{2}C_{ijkl}e_{ij}e_{kl} = \tfrac{1}{2}C_{ijkl}\left(\varepsilon_{ij} - \varepsilon_{ij}^0\right)\left(\varepsilon_{kl} - \varepsilon_{kl}^0\right), \tag{6}$$

where e_{ij}, C_{ijkl}, ε_{ij}, and ε_{ij}^0, denote elastic strain, elastic stiffness tensor, total strain, and eigenstrain, respectively. The eigenstrain is described by $\varepsilon_{ij}^0 = Q_{ijkl}P_iP_j$; Q_{ijkl} denotes the electrostrictive coefficient.

For freestanding bilayers and superlattice systems, we assume that the total strain ε_{ij} is homogeneous in bilayers; then the total strain ε_{ij} is equal to the lattice misfit strain $\varepsilon_{\mathrm{latt}}$ [41]. For superlattice systems with a STO substrate, the misfit strains of the PTO and STO layers can be expressed by $\varepsilon_{\mathrm{S}}^{\mathrm{P}} = (a_{\mathrm{S}}–a_{\mathrm{P}})/a_{\mathrm{S}}$ and $\varepsilon_{\mathrm{S}}^{\mathrm{S}} = 0$, where $\varepsilon_{\mathrm{S}}^{\mathrm{P}}$ and $\varepsilon_{\mathrm{S}}^{\mathrm{S}}$ denote the misfit strain of the PTO and STO layers from the superlattice, respectively. Due to the difference of lattice constants between pseudocubic PTO and cubic STO, misfit strain is derived from the deformation of a single layer to its reference state:

$$\varepsilon_{\mathrm{F}}^{\mathrm{P}} = \frac{a_{\mathrm{ref}} - a_{\mathrm{P}}}{a_{\mathrm{P}}}, \tag{7}$$

$$\varepsilon_{\mathrm{F}}^{\mathrm{S}} = \frac{a_{\mathrm{ref}} - a_{\mathrm{S}}}{a_{\mathrm{S}}}, \tag{8}$$

where $\varepsilon_{\mathrm{F}}^{\mathrm{P}}$ and $\varepsilon_{\mathrm{F}}^{\mathrm{S}}$ represent the misfit strain in the PTO and STO layers from the freestanding bilayers; a_{P}, a_{S}, and a_{ref} denote the lattice constant of PTO and STO, and the reference lattice constant of the as-grown bilayers, respectively. For the unreleased as-grown bilayers on the substrate, a_{ref} is set as the lattice parameter of the STO substrate, i.e., $a_{\mathrm{ref}} = a_{\mathrm{S}}$. For the released bilayers, the reference lattice constant can be described from previous research [42]:

$$a_{\mathrm{ref}} = \frac{a_{\mathrm{P}}h_{\mathrm{P}} + a_{\mathrm{S}}h_{\mathrm{S}}}{h_{\mathrm{P}} + h_{\mathrm{S}}}, \tag{9}$$

where h_{P} and h_{S} are the thickness of the PTO and STO layers, respectively.

The mechanical equilibrium $\sigma_{ij,j} = 0$ and electric equilibrium equation $D_{i,i} = 0$ will be satisfied at the vacuum interface of the freestanding bilayers, in which stress is expressed by

$$\sigma_{ij} = C_{ijkl}\, e_{kl} = C_{ijkl}\left(\varepsilon_{kl} - \varepsilon_{kl}^0\right), \tag{10}$$

while the local electric displacement is

$$D_i = \varepsilon_0\chi_{ij}E_j + P_i. \tag{11}$$

In this work, a finite element method was performed to solve Eq. (1), and a mesh of 48 × 48 × 8 was employed for the discrete PTO layer and 48 × 48 × 4 for the STO layer for $(\mathrm{PTO})_{20}/(\mathrm{STO})_{10}$, where the grid length is 1.0 nm. When performing simulations in freestanding films with different PTO thicknesses, the PTO layer was meshed by $120 \times 120 \times N$, where N was the same number of unit cells as the PTO layer thickness. The same grid length as $\mathrm{PTO}_{20}/\mathrm{STO}_{10}$ was employed in these models. In freestanding films, the periodic boundary condition was applied along the x and y directions. An open-circuit surface boundary condition was employed on the top and bottom interfaces to solve Eq. (5). Meanwhile, for simplicity, the model for the PTO/STO superlattice system was established with one $(\mathrm{PTO})_{20}/(\mathrm{STO})_{10}$ period, while a periodical boundary condition for polarization vector $\vec{\boldsymbol{P}} = (P_x, P_y, P_z)$ along the z direction was applied to simulate one superlattice period in a real superlattice system. An open-current electric boundary condition was used on the top and bottom interfaces of this $(\mathrm{PTO})_{10}/(\mathrm{STO})_{20}$ period. The misfit strain was set at two interfaces on both sides of the PTO layer, while the strain in the STO layer was set as zero. A random initial noise of polarization was used in the superlattice and freestanding models for these simulations at room temperature, with a peak amplitude of $0.005\,\mathrm{C/m^2}$. The material constants were obtained from previous work [43,44]. The lattice parameters of pseudocubic PTO and cubic STO were chosen as 3.955 and 3.905 Å [45]. In addition, skyrmion bubbles can be characterized by the topological number, i.e.,

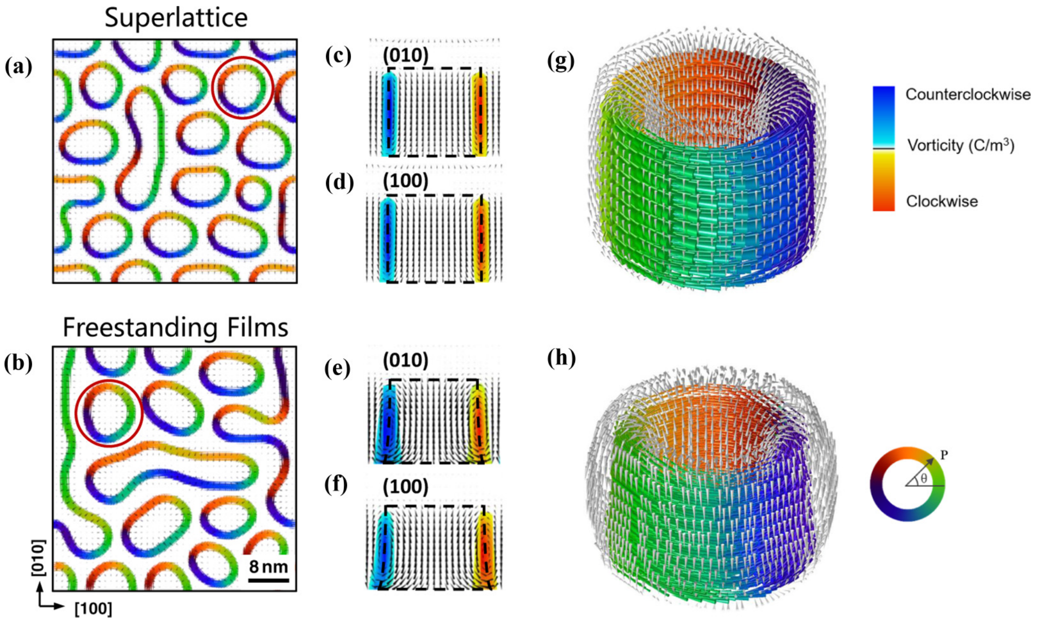

FIG. 1. Ferroelectric domains of $(\text{PTO})_{20}/(\text{STO})_{10}$ superlattice on the SrTiO_3 substrate and PTO/STO freestanding bilayers. (a,b) are planar views of ferroelectric domains in PTO/STO superlattice and freestanding films. The cross-sectional views of polar texture and vorticity of a skyrmion domain wall in superlattice (c,d), and freestanding film (e,f), which are circled in red in (a,b). Dashed lines depict the shape of the skyrmion bubbles. Orange/blue color scale indicates the core of domain walls along the [010] or [100] direction. (g,h) are the three-dimensional (3D) configuration of a skyrmion bubble circled in (a,b). The gray arrows depict the polarization distribution and the spectrum color arrows demonstrate the skyrmion domain walls. The color represents the IP polarization orientations.

skyrmion number N_{SK} [46]:

$$N_{\text{SK}} = \frac{1}{4\pi}\int \boldsymbol{q}\,dxdy = \frac{1}{4\pi}\int \boldsymbol{u}\cdot\left(\frac{\partial \boldsymbol{u}}{\partial x}\times\frac{\partial \boldsymbol{u}}{\partial y}\right)dxdy, \quad (12)$$

where $\boldsymbol{u}$ denotes the normalized local dipole moment; $\boldsymbol{q}$ denotes the local Pontryagin density. The surface integral domain is acquired from the [001] plane at the PTO/STO interface.

III. RESULTS AND DISCUSSIONS

To preliminarily explore skyrmion bubbles in the freestanding films, we performed the simulation in both superlattice and freestanding films for comparison. Figure 1(a) displays the top view of the domain pattern in the PTO/STO superlattice, which reveals a higher density of isolated skyrmion bubbles in the superlattice (corresponding skyrmion number $N_{\text{SK}} = 17$) [9,15]. Meanwhile, as shown in Fig. 1(b), the freestanding bilayers show the coexistence of isolated skyrmion bubbles and elongated states ($N_{\text{SK}} = 11$) [47]. Usually, the skyrmion bubbles, especially isolated ones, are energetically unfavored, which is mainly derived from a built-in electric field or strain/strain gradient. The observations demonstrate the critical role of the compressive strain distribution in creating and stabilizing more isolated skyrmion bubbles in the PTO layer [48–50]. Figures 1(c)–1(f) display the IP polar texture of the isolated skyrmion bubbles in the superlattice and freestanding bilayers, respectively. Both systems display vortex-antivortex (VAV) pairs from the cross-sectional views, but skyrmion bubbles in the superlattice are more cylindrical while those in the freestanding bilayers resemble a truncated cone, as shown in Figs. 1(g) and 1(h). The reason is that the screening effect at the PTO/vacuum interface produces a higher local depolarization field than the PTO/STO interface, giving rise to more polarization rotation into the planar direction [51]. These truncated cone-shape skyrmion bubbles were experimentally discovered in a pioneering work by Han *et al.* [38]. It is worth noting that the size and shape of the observed center-divergent domains are highly consistent with our simulation. The details of a simulated skyrmion bubble are shown in Supplemental Fig. 1 in the Supplemental Material [52].

To further understand the nature of the skyrmion bubbles in freestanding bilayers, we proceeded with the simulation of the domain evolution by varying the PTO layer thickness. Figure 2(a) depicts the IP polarization of the topological domains in the $(\text{PTO})_m/(\text{STO})_{10}$ bilayers in different PTO layer thicknesses. As the thickness gradually increases from 2 to 50 u.c., we found that the domains undergo configuration transitions from *a*/*c* domains to skyrmion bubbles, then to flux-closure.

Then we plotted the energy variations dependent on the PTO layer to analyze the reason for the formation of these topological domains, as depicted in Fig. 2(b). The total energy decreases monotonously with thickness, which mainly originates from the reduced Landau and elastic energy. For $m < 8$ u.c., the PTO layer holds a strong depolarization field, and a dense *a*/*c* domain with alternating ferroelastic domain emerges, which results from the dominant elastic energy in the PTO layer. Meanwhile, due to the growth of the *z*-directional polarization and the emergence of the skyrmion bubble state, the electrostatic and gradient energy slightly increase initially. As the thickness reaches 8 u.c., the skyrmion bubbles are created due to the weakened depolarization, while the gradient

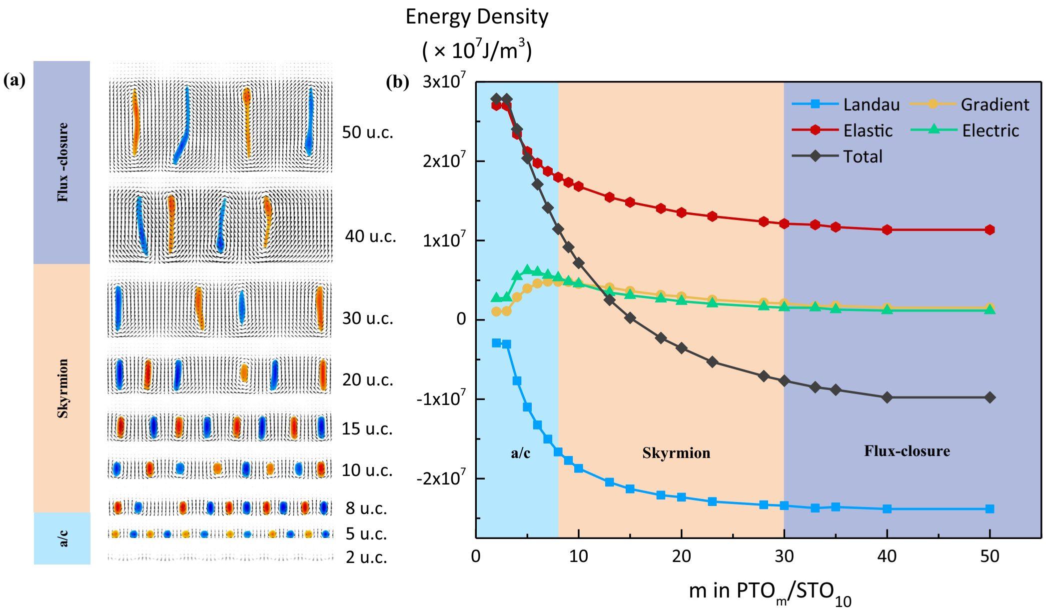

FIG. 2. Domain evolution by varying PTO thickness. (a) IP polarization configuration of ferroelectric domains in $\mathrm{PTO}_m/\mathrm{STO}_{10}$ with $m = 2, 5, 8, 10, 15, 20, 30, 40, 50$. (b) Various energy densities in PTO layer as the function of thickness m in $\mathrm{PTO}_m/\mathrm{STO}_{10}$.

energy also decreases with the increase of thickness. If the thickness increases more ($8\,\mathrm{u.c.} < m < 30\,\mathrm{u.c.}$), the Landau energy and elastic energy keep decreasing, but the compressive strain still maintains the stabilization of the skyrmion bubbles. When $m > 30\,\mathrm{u.c.}$, the epitaxial strain decreases continually, while the depolarization field is weaker. The lack of these two energy resources leads to the transformation of the skyrmion bubbles to a flux-closure domain. Such flux-closure domains are consistent with the domains observed in Co/PTO/LSMO/STO heterojunctions [53]. In addition, a similar energy evolutionary trend has been demonstrated in previous simulations in a $\mathrm{PbTiO_3/SrTiO_3}$ superlattice on a $\mathrm{DyScO_3}$(DSO) substrate [50,54].

Compared to superlattice structure, freestanding films provide a continuously strain-tunable platform. Therefore, we explored the evolution of the skyrmion bubbles in the presence of the IP uniaxial and biaxial strains. The IP strain was increased (decreased) from 0% to 1.5% (–1.5%) with steps of 0.05% (–0.05%); the time of every step was set as 500 ns. Then the strain was released with the same step length until the bilayers fully relaxed. The evolution of the skyrmion bubbles under uniaxial compressive strain is given in Figs. 3(b) and 3(c), with the initial state in Fig. 3(a). With the application of compressive strain, the skyrmion domain walls exhibit IP motion through the PTO layer and slowly consolidate into elongated stripes along the direction of applied strain, which can be characterized by the variation of skyrmion number N_{SK} [see Fig. 3(f)]. This tendency persists until the tensile strain reaches -1.3% and remains unchanged at a higher strain. This phenomenon may have two origins: (1) Due to the electrostrictive coupling, the compressive strain rotate the IP polarization of skyrmion bubbles in the strain direction. (2) The skyrmion bubbles are also stabilized by the depolarization field in the PTO layer under the applied strain. Based on these two factors, skyrmion bubbles start to consolidate and elongate under compressive strain and do not transform into normal ferroelectric domains. Furthermore, the skyrmion domain walls portray a zigzag configuration with 90° when strain is removed, according to Figs. 3(b) and 3(c). This phenomenon mainly derives from the zigzag arrangement reducing elastic energy, resembling the formation of 90° domain walls [55].

The motion of skyrmion domain walls under uniaxial tensile strain is given in Figs. 4(a)–4(e), which characterizes a distinguishable evolutionary behavior. To better probe the evolutionary behavior of skyrmion bubbles, we apply the tensile strain along the [010] direction. As the strain increases to $\varepsilon_{22} = 0.1\%$, the skyrmion domain walls start to consolidate and elongate along the [100] direction, i.e., the direction perpendicular to the applied strain. When the neighboring skyrmion domain walls consolidate, the VAV pairs approach each other along the lateral direction. Then the consolidation of skyrmion domain walls begins near the PTO/vacuum interface [Fig. 4(g)], and eventually leads to the annihilation of the VAV pairs. As ε_{22} increases, the isolated skyrmion bubbles gradually transform into long stripes. As ε_{22} reaches to 0.35%, the elongated stripes can be clearly observed from the planar view [Fig. 4(c)]. With the further increase of ε_{22}, these elongated stripes do not display obvious lateral motion in the PTO layer. However, as shown in Supplemental Figs. 3(a)–3(c) [52], the cross-sectional images reveal that the VAV pairs start to move away from each other along the z direction towards vacuum and STO interfaces, ready to form so-called periodic dipole waves in ferroelectric oxide structures [56]. Strain-induced IP polarization growth in different regions along [010] and $[0\bar{1}0]$ is responsible for this behavior [26]. It should be noted that the polarization along the [010] and $[0\bar{1}0]$ directions also involves rapid polarization variation at their interfaces, giving rise to the growth of gradient energy and calculated N_{SK} in the PTO layer. When the strain increases to the critical value ($\varepsilon_{22} = 0.9\%$), skyrmion bubbles are fully transferred into elongated stripes, as shown in Fig. 4(d).

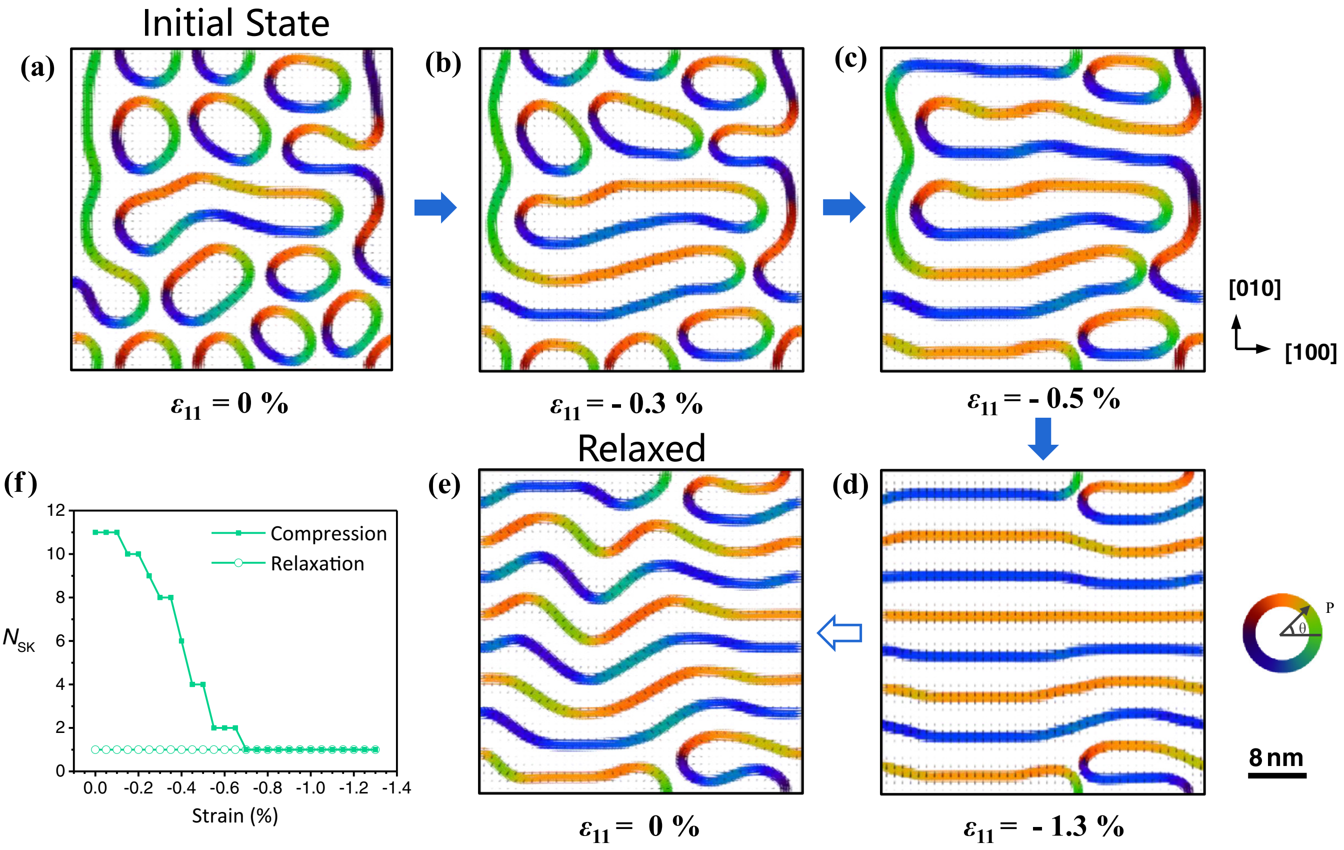

FIG. 3. Ferroelectric domain evolution under the uniaxial compression along [010]. (a) Initial skyrmion bubbles in freestanding bilayers. Skyrmion bubbles gradually transfer into long stripes before compressive strain increases up to –1.3% (b–d), and then transfer into zigzag configuration when strain is released (e). (f) Dependence of skyrmion number N_{SK} on in-plane compressive strain. During the compressive strain, the skyrmion number drops with the consolidation of neighboring skyrmion bubbles.

Note that when strain increases beyond the critical value, the skyrmion domain walls are driven towards the PTO/STO or PTO/vacuum interface and annihilated (see Supplemental Fig. 3(e) in the Supplemental Material [52]). Further increasing strain erases most topological domains, which eventually transfer into a_1/a_2 ferroelectric 180° domains [57,58]. Inevitably, as given in Supplemental Fig. 3(e) [52], a few vortices remain in the PTO layer near the PTO/vacuum interface. In further simulation, these remaining vortices still exist even though tensile strain increases up to 3%. If the tensile strain is removed at the a_1/a_2 ferroelectric domains stage, skyrmion bubbles would be returned with random distribution, as presented in Fig. 4(j). Conversely, if the strain is removed at or below critical strain, the skyrmion bubbles stop consolidating and eventually transform into long stripes. In addition, a distinguishable vortex domain is observed in the PTO/STO superlattice on a DSO substrate [5]; the skyrmion bubbles also exhibit a zigzag arrangement as they relax from compressive strain [55].

To further investigate the strain manipulation of the skyrmion bubbles, we also explored the evolutionary behavior under the biaxial strain. Under biaxial tensile strain, the skyrmion bubbles undergo a similar result as that under uniaxial tension. Skyrmion bubbles transfer into a_1/a_2 twin domains and return to a random state of skyrmion bubbles [Figs. 5(b) and 5(c)] after strain relaxation. Under biaxial compressive strain, Neél components of the skyrmion domain walls decrease and further reduce the size of the skyrmion bubbles. Compared with the PTO thin films at room temperature, which completely transform into c domains when biaxial misfit strain increases beyond 1.5% [59], the vortex structure of the skyrmion domain walls is instead maintained by the depolarization field. Moreover, it is observed that Fig. 5(d) does not display significant changes compared to Fig. 5(a). This is mainly because biaxial compression induces the IP polarization rotate into the z directions in our simulation. There are few IP polarization components involved in the rotation along the (001) plane. However, this rotation of IP polarization, especially on the skyrmion domain walls, is the main reason for the rearrangement of skyrmion bubbles. Thus, the configuration of skyrmion bubbles does not change significantly under biaxial compression.

In general, we conclude that not only compression but also tension induces elongation and consolidation of skyrmion bubbles in freestanding PTO/STO films. However, the difference is that this process induced by compressive strain is along the perpendicular direction of applied strain, while that induced by tensile strain is along the direction of applied strain, as shown in Figs. 3 and 4. It should be noted that if tensile strain increases beyond the critical strain ($\varepsilon_{11} = 0.9\%$), the skyrmion bubbles would return with random distribution after strain is released. If not, the

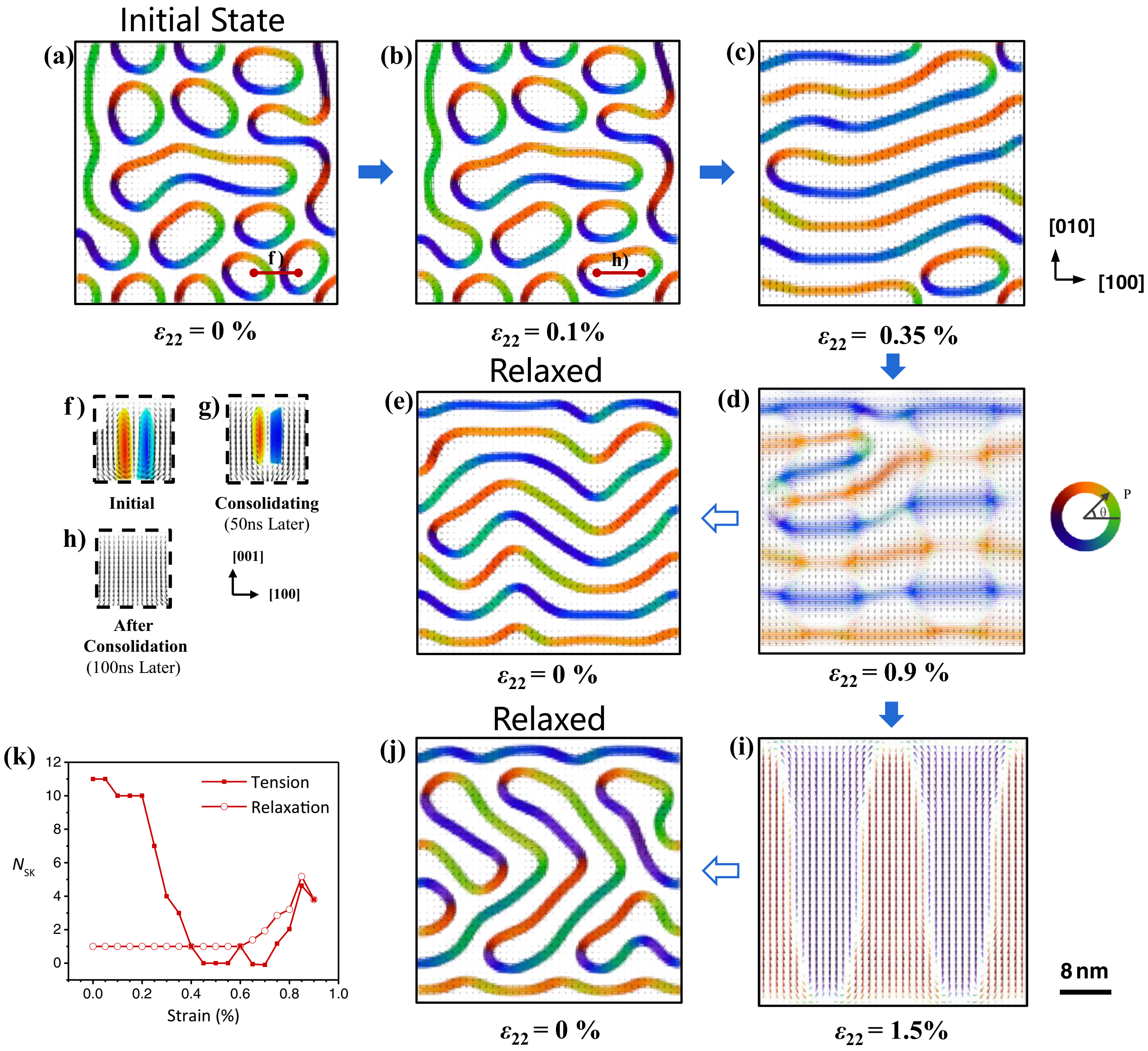

FIG. 4. Ferroelectric domain evolution under the uniaxial tensile strain along [100]. (a) Initial skyrmion bubbles in freestanding bilayers. Skyrmion bubbles start to consolidate with the growth of strain ε_{22} (b,c) and start to vanish when tensile strain increases beyond 0.9% (d), and then are re-created after strain is released (e). (f–h) Cross-sectional views of the consolidation process of a pair of neighboring skyrmion domain walls. (i) a_1/a_2 ferroelectric domain patterns under further increase of uniaxial tensile strain reaching to 1.5%, and returning to a normal skyrmion bubble state (j). (k) Dependence of skyrmion number N_{SK} on in-plane tensile strain.

skyrmion bubbles would transform into elongated stripes. Meanwhile, biaxial tension induces a topological phase transition from skyrmion bubbles into a_1/a_2 twin domains and returns with a random distribution of skyrmion bubbles after strain relaxation, but there is no significant change of configuration of the skyrmion bubbles under biaxial tension.

Furthermore, as shown in Figs. 6(a)–6(e), we performed the simulation of skyrmion bubbles at varying temperature under strain-free state, while the corresponding thermal expansion was neglected. At the beginning of the temperature growth, the topology of skyrmion bubbles does not display significant changes, as shown in Figs. 6(a) and 6(b). This phenomenon is in accordance with the experimental results in a superlattice system [19]. When the temperature increases above 600 K, the neighboring skyrmion bubbles start to consolidate with each other. The reason is as follows: For a biaxial-compressed PTO layer, IP polarization of Neél type domain walls is energetically unfavorable at a high-temperature ferroelectric state (i.e., the state between 600 K and T_c) [60], which decreases the IP polarization to reduce the Landau energy. Then the area of vortex domain walls shrinks, leading to the consolidation of skyrmion bubbles. As the temperature reaches 805 K, stripe domains are erased, as shown in Fig. 6(e). Meanwhile, N_{SK} of a skyrmion bubble is calculated, as shown in Fig. 6(f).

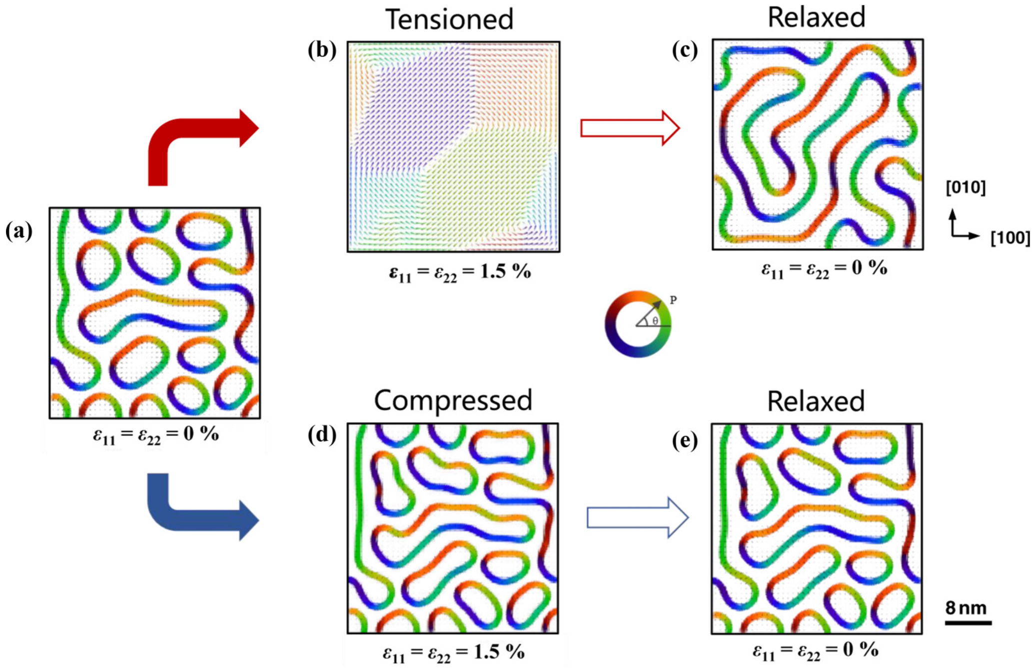

FIG. 5. Evolution of ferroelectric domain patterns from initial state (a) under biaxial tensile strain (b) and biaxial compressive strain (d) with corresponding relaxed states, as presented in (c) and (e) respectively. Color arrows in (b) demonstrates IP ferroelectric polarizations orientations, as shown in the color wheel.

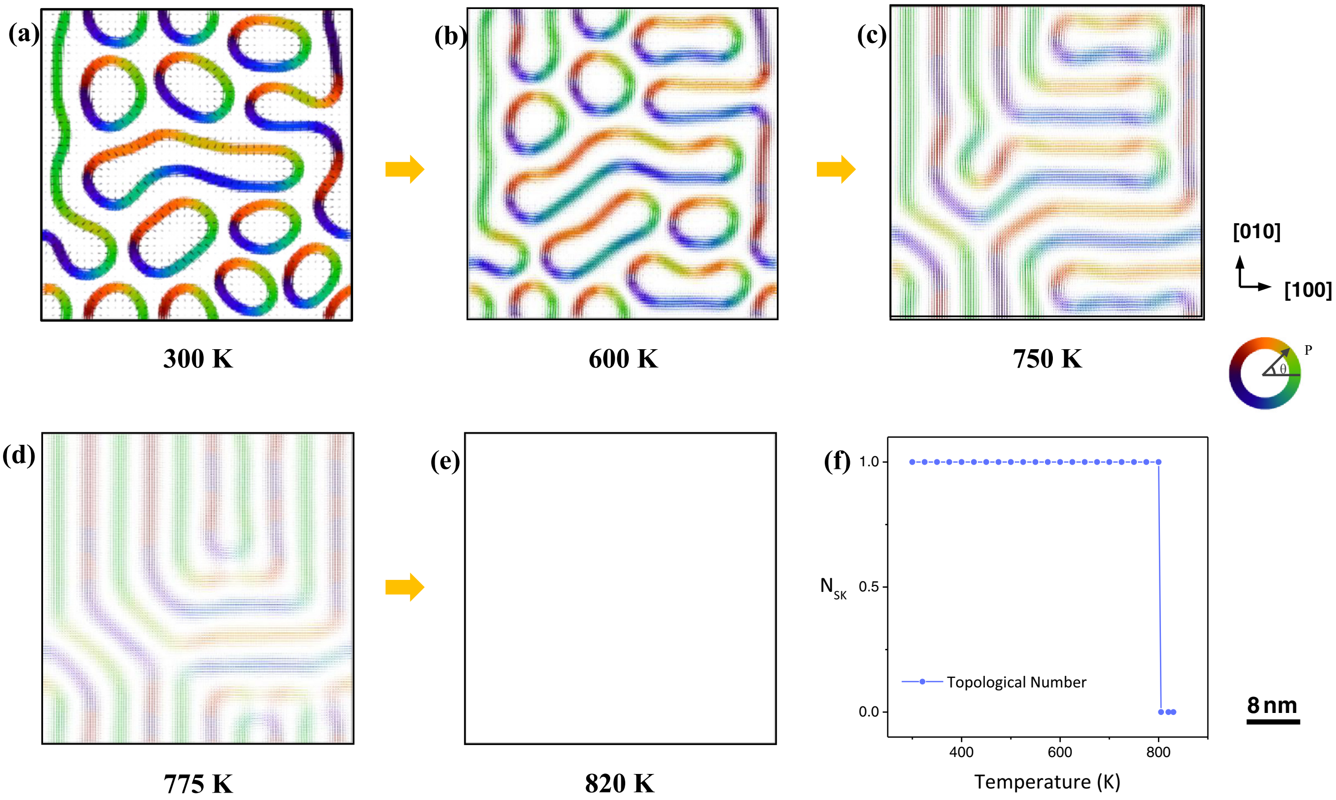

FIG. 6. Temperature-dependent domain evolution under the same strain. (a–e) The skyrmion bubbles in PTO layer at 300, 600, 750, 775, and 820 K. (f) Skyrmion number N_{SK} of a skyrmion bubble and its consolidated state in dependence on the temperature.

IV. CONCLUSIONS

In conclusion, we observed ferroelectric skyrmion bubbles in PTO/STO freestanding bilayer systems from phase field simulations. Because of the high depolarization effect induced by asymmetric interface and misfit strain, isolated skyrmion bubbles denotes a truncated cone shape in the PTO layer. Stemming from the domination of elastic energy and Landau energy interacting, topological domains in $\mathrm{PTO}_m/\mathrm{STO}_{10}$ exhibit a transition from *a*/*c* domain to skyrmion bubbles, and finally flux closure with varying PTO thickness. Then the manipulation behavior of uniaxial strain is explored, which shows that tensile strain induced skyrmion bubble consolidation occurs along the direction of applied strain, while compressive strain induces consolidation perpendicular to the direction of applied strain. This process is derived from the energy competition of Landau energy and elastic energy. Meanwhile, ferroelectric skyrmion bubbles are transferred into a_1/a_2 ferroelectric domains when strain increases higher than the critical strain. Our results provide a detailed study of the configuration and operation of polar topological domains in freestanding bilayers, which gives us an avenue to the development of novel electronic and memory devices on freestanding films.

ACKNOWLEDGMENTS

This work at Beijing Institute of Technology was supported by the National Key Research and Development Program of China (Grant No. 2019YFA0307900), the National Natural Science Foundation of China (Grants No. 12172047, No. 92163101, and No. 11804023), and Beijing Natural Science Foundation (Grant No. Z190011).

---

[1] Y. Liu, Y. J. Wang, Y. L. Zhu, C. H. Lei, Y. L. Tang, S. Li, S. R. Zhang, J. Li, and X. L. Ma, Large scale two-dimensional flux-closure domain arrays in oxide multilayers and their controlled growth, Nano Lett. **17**, 7258 (2017).

[2] C. L. Jia, K. W. Urban, M. Alexe, D. Hesse, and I. Vrejoiu, Direct observation of continuous electric dipole rotation in flux-closure domains in ferroelectric $\mathrm{Pb(Zr, Ti)O_3}$, Science **331**, 1420 (2011).

[3] W. J. Chen and Y. Zheng, Vortex switching in ferroelectric nanodots and its feasibility by a homogeneous electric field: Effects of substrate, dislocations and local clamping force, Acta Mater. **88**, 41 (2015).

[4] Y. L. Tang, Y. L. Zhu, X. L. Ma, A. Y. Borisevich, A. N. Morozovska, E. A. Eliseev, W. Y. Wang, Y. J. Wang, Y. B. Xu, Z. D. Zhang, and S. J. Pennycook, Observation of a periodic array of flux-closure quadrants in strained ferroelectric $\mathrm{PbTiO_3}$ films, Science **348**, 547 (2015).

[5] A. K. Yadav, C. T. Nelson, S. L. Hsu, Z. Hong, J. D. Clarkson, C. M. Schlepütz, A. R. Damodaran, P. Shafer, E. Arenholz, L. R. Dedon, D. Chen, A. Vishwanath, A. M. Minor, L. Q. Chen, J. F. Scott, L. W. Martin, and R. Ramesh, Observation of polar vortices in oxide superlattices, Nature (London) **530**, 198 (2016).

[6] Y. T. Chen, Y. L. Tang, Y. L. Zhu, Y. J. Wang, M. J. Han, M. J. Zou, Y. P. Feng, W. R. Geng, F. H. Gong, and X. L. Ma, Periodic Vortex-Antivortex Pairs in Tensile Strained $\mathrm{PbTiO_3}$ Films, Appl. Phys. Lett. **117**, 192901 (2020).

[7] D. Karpov, Z. Liu, T. dos Santos Rolo, R. Harder, P. V. Balachandran, D. Xue, T. Lookman, and E. Fohtung, Three-dimensional imaging of vortex structure in a ferroelectric nanoparticle driven by an electric field, Nat. Commun. **8**, 280 (2017).

[8] A. Y. Abid, Y. Sun, X. Hou, C. Tan, X. Zhong, R. Zhu, H. Chen, K. Qu, Y. Li, M. Wu, J. Zhang, J. Wang, K. Liu, X. Bai, D. Yu, X. Ouyang, J. Wang, J. Li, and P. Gao, Creating polar antivortex in $\mathrm{PbTiO_3/SrTiO_3}$ superlattice, Nat. Commun. **12**, 2054 (2021).

[9] S. Das, Y. L. Tang, Z. Hong, M. A. P. Goncalves, M. R. McCarter, C. Klewe, K. X. Nguyen, F. Gomez-Ortiz, P. Shafer, E. Arenholz, V. A. Stoica, S. L. Hsu, B. Wang, C. Ophus, J. F. Liu, C. T. Nelson, S. Saremi, B. Prasad, A. B. Mei, D. G. Schlom *et al.*, Observation of room-temperature polar skyrmions, Nature (London) **568**, 368 (2019).

[10] Z. Hong and L.-Q. Chen, Blowing polar skyrmion bubbles in oxide superlattices, Acta Mater. **152**, 155 (2018).

[11] M. A. P. Gonçalves, C. Escorihuela-Sayalero, P. Garca-Fernández, J. Junquera, and J. Íñiguez, Theoretical guidelines to create and tune electric skyrmion bubbles, Sci. Adv. **5**, eaau7023 (2019).

[12] J. Hong, G. Catalan, D. N. Fang, E. Artacho, and J. F. Scott, Topology of the polarization field in ferroelectric nanowires from first principles, Phys. Rev. B **81**, 172101 (2010).

[13] Y. J. Wang, Y. P. Feng, Y. L. Zhu, Y. L. Tang, L. X. Yang, M. J. Zou, W. R. Geng, M. J. Han, X. W. Guo, B. Wu, and X. L. Ma, Polar meron lattice in strained oxide ferroelectrics, Nat. Mater. **19**, 881 (2020).

[14] Y. Nahas, S. Prokhorenko, J. Fischer, B. Xu, C. Carrétéro, S. Prosandeev, M. Bibes, S. Fusil, B. Dkhil, V. Garcia, and L. Bellaiche, Inverse transition of labyrinthine domain patterns in ferroelectric thin films, Nature (London) **577**, 47 (2020).

[15] S. Das, Z. Hong, V. A. Stoica, M. A. P. Goncalves, Y. T. Shao, E. Parsonnet, E. J. Marksz, S. Saremi, M. R. McCarter, A. Reynoso, C. J. Long, A. M. Hagerstrom, D. Meyers, V. Ravi, B. Prasad, H. Zhou, Z. Zhang, H. Wen, F. Gomez-Ortiz, P. Garcia-Fernandez *et al.*, Local negative permittivity and topological phase transition in polar skyrmions, Nat. Mater. **20**, 194 (2021).

[16] A. K. Yadav, K. X. Nguyen, Z. Hong, P. Garcia-Fernandez, P. Aguado-Puente, C. T. Nelson, S. Das, B. Prasad, D. Kwon, S. Cheema, A. I. Khan, C. Hu, J. Iniguez, J. Junquera, L. Q. Chen, D. A. Muller, R. Ramesh, and S. Salahuddin, Spatially resolved steady-state negative capacitance, Nature (London) **565**, 468 (2019).

[17] P. Zubko, J. C. Wojdel, M. Hadjimichael, S. Fernandez-Pena, A. Sene, I. Luk'yanchuk, J. M. Triscone, and J. Iniguez, Negative capacitance in multidomain ferroelectric superlattices, Nature (London) **534**, 524 (2016).

[18] Y. Ji, W. J. Chen, and Y. Zheng, The emergence of tunable negative electrocaloric effect in ferroelectric/paraelectric superlattices, J. Phys. D: Appl. Phys. **53**, 505302 (2020).

[19] Y.-T. Shao, S. Das, Z. Hong, R. Xu, S. Chandrika, F. GómezOrtiz, P. García-Fernández, L.-Q. Chen, H. Y. Hwang,

J. Junquera, L. W. Martin, R. Ramesh, and D. A. Muller, Emergent chirality in a polar meron to skyrmion phase transition, arXiv:2101.04545.

[20] P. Shafer, P. Garcia-Fernandez, P. Aguado-Puente, A. R. Damodaran, A. K. Yadav, C. T. Nelson, S. L. Hsu, J. C. Wojdel, J. Iniguez, L. W. Martin, E. Arenholz, J. Junquera, and R. Ramesh, Emergent chirality in the electric polarization texture of titanate superlattices, Proc. Natl. Acad. Sci. USA. **115**, 915 (2018).

[21] Y. Deng, C. Gammer, J. Ciston, P. Ercius, C. Ophus, K. Bustillo, C. Song, R. Zhang, D. Wu, Y. Du, Z. Chen, H. Dong, A. G. Khachaturyan, and A. M. Minor, Hierarchically-structured large superelastic deformation in ferroelastic-ferroelectrics, Acta Mater. **181**, 501 (2019).

[22] S. Yuan, W. J. Chen, L. L. Ma, Y. Ji, W. M. Xiong, J. Y. Liu, Y. L. Liu, B. Wang, and Y. Zheng, Defect-mediated vortex multiplication and annihilation in ferroelectrics and the feasibility of vortex switching by stress, Acta Mater. **148**, 330 (2018).

[23] D. Kuzum, S. Yu, and H.-S. P. Wong, Synaptic electronics: Materials, devices and applications, Nanotechnology **24**, 382001 (2013).

[24] J. Ma, J. Ma, Q. Zhang, R. Peng, J. Wang, C. Liu, M. Wang, N. Li, M. Chen, X. Cheng, P. Gao, L. Gu, L. Q. Chen, P. Yu, J. Zhang, and C. W. Nan, Controllable conductive readout in self-assembled, topologically confined ferroelectric domain walls, Nat. Nanotechnol. **13**, 947 (2018).

[25] Q. Li, V. A. Stoica, M. Pasciak, Y. Zhu, Y. Yuan, T. Yang, M. R. McCarter, S. Das, A. K. Yadav, S. Park, C. Dai, H. J. Lee, Y. Ahn, S. D. Marks, S. Yu, C. Kadlec, T. Sato, M. C. Hoffmann, M. Chollet, M. E. Kozina *et al.*, Subterahertz collective dynamics of polar vortices, Nature (London) **592**, 376 (2021).

[26] T. Yang, C. Dai, Q. Li, H. Wen, and L.-Q. Chen, Condensation of collective polar vortex modes, Phys. Rev. B **103**, L220303 (2021).

[27] W. Yang, G. Tian, Y. Zhang, F. Xue, D. Zheng, L. Zhang, Y. Wang, C. Chen, Z. Fan, Z. Hou, D. Chen, J. Gao, M. Zeng, M. Qin, L. Q. Chen, X. Gao, and J. M. Liu, Quasi-one-dimensional metallic conduction channels in exotic ferroelectric topological defects, Nat. Commun. **12**, 1306 (2021).

[28] W. Sun, W. Wang, H. Li, G. Zhang, D. Chen, J. Wang, and Z. Cheng, Controlling bimerons as skyrmion analogues by ferroelectric polarization in 2D van der Waals multiferroic heterostructures, Nat. Commun. **11**, 5930 (2020).

[29] J. Yin, H. Zong, H. Tao, X. Tao, H. Wu, Y. Zhang, L. D. Zhao, X. Ding, J. Sun, J. Zhu, J. Wu, and S. J. Pennycook, Nanoscale bubble domains with polar topologies in bulk ferroelectrics, Nat. Commun. **12**, 3632 (2021).

[30] L. Van Lich, M.-T. Le, N.-L. Vu, H.-D. Nguyen, V.-T. Le, M.-T. Ha, T.-G. Nguyen, and V.-H. Dinh, Direct switching of polarization vortex in triangular ferroelectric nanodots: Role of crystal orientation, Phys. Rev. B **104**, 024104 (2021).

[31] I. I. Naumov, L. Bellaiche, and H. Fu, Unusual phase transitions in ferroelectric nanodisks and nanorods, Nature **432**, 737 (2004).

[32] A. Baghizadeh, J. M. Vieira, P. Mirzadeh Vaghefi, M. G. Willinger, and V. S. Amaral, Development of ferroelectric domains and topological defects in vacancy doped ceramics of *h*-$\mathrm{LuMnO_3}$, J. Appl. Phys. **122**, 044102 (2017).

[33] G. Dong, S. Li, M. Yao, Z. Zhou, Y.-Q. Zhang, X. Han, Z. Luo, J. Yao, B. Peng, Z. Hu, H. Huang, T. Jia, J. Li, W. Ren, Z.-G. Ye, X. Ding, J. Sun, C.-W. Nan, L.-Q. Chen, J. Li *et al.*, Superelastic ferroelectric single-crystal membrane, Science **366**, 475 (2019).

[34] H. S. Kum, H. Lee, S. Kim, S. Lindemann, W. Kong, K. Qiao, P. Chen, J. Irwin, J. H. Lee, S. Xie, S. Subramanian, J. Shim, S. H. Bae, C. Choi, L. Ranno, S. Seo, S. Lee, J. Bauer, H. Li, K. Lee *et al.*, Heterogeneous integration of single-crystalline complex-oxide membranes, Nature (London) **578**, 75 (2020).

[35] S. S. Hong, M. Gu, M.Verma, V. Harbola, B. Y. Wang, D. Lu, A. Vailionis, Y. Hikita, R. Pentcheva, J. M. Rondinelli, and H. Y. Hwang, Extreme tensile strain states in $\mathrm{La_{0.7}Ca_{0.3}MnO_3}$ membranes, Science **368**, 71 (2020).

[36] S. Cai, Y. Lun, D. Ji, L. Han, C. Guo, Y. Zang, S. Gao, Y. Wei, M. Gu, C. Zhang, Z. Gu, X. Wang, C. Addiego, D. Fang, Y. Nie, J. Hong, P. Wang, and X. Pan, Giant polarization and abnormal flexural deformation in bent freestanding perovskite oxides, arXiv:2009.03177.

[37] S. R. Bakaul, S. Prokhorenko, Q. Zhang, Y. Nahas, Y. Hu, A. Petford-Long, L. Bellaiche, and N. Valanoor, Freestanding ferroelectric bubble domains, Adv. Mater. **33**, 2105432 (2021).

[38] L. Han, C. Addiego, S. Prokhorenko, M. Wang, H. Fu, Y. Nahas, X. Yan, S. Cai, T. Wei, Y. Fang, H. Liu, D. Ji, W. Guo, Z. Gu, Y. Yang, P. Wang, L. Bellaiche, Y. Chen, D. Wu, Y. Nie *et al.*, High-density switchable skyrmion-like polar nanodomains integrated on silicon, Nature (London) **603**, 63 (2022).

[39] Y. Wang, J. Sun, T. Shimada, H. Hirakata, T. Kitamura, and J. Wang, Ferroelectric control of magnetic skyrmions in multiferroic heterostructures, Phys. Rev. B **102**, 014440 (2020).

[40] J. Wang, Y. Shi, and M. Kamlah, Uniaxial strain modulation of the skyrmion phase transition in ferromagnetic thin films, Phys. Rev. B **97**, 024429 (2018).

[41] Y. L. Li, S. Y. Hu, Z. K. Liu, and L. Q. Chen, Effect of substrate constraint on the stability and evolution of ferroelectric domain structures in thin films, Acta Mater. **50**, 395 (2002).

[42] F. Xue, J. J. Wang, G. Sheng, E. Huang, Y. Cao, H. H. Huang, P. Munroe, R. Mahjoub, Y. L. Li, V. Nagarajan, and L. Q. Chen, Phase field simulations of ferroelectrics domain structures in $\mathrm{PbZr}_x\mathrm{Ti}_{1-x}\mathrm{O}_3$ bilayers Acta Mater. **61**, 2909 (2013).

[43] M. J. Haun, E. Furman, S. J. Jang, H. A. McKinstry, and L. E. Cross, Thermodynamic theory of $\mathrm{PbTiO_3}$, J. Appl. Phys. **62**, 3331 (1987).

[44] G. Sheng, Y. L. Li, J. X. Zhang, S. Choudhury, Q. X. Jia, V. Gopalan, D. G. Schlom, Z. K. Liu, and L. Q. Chen, A modified Landau–Devonshire thermodynamic potential for strontium titanate, Appl. Phys. Lett. **96**, 232902 (2010).

[45] Q. Li, C. T. Nelson, S.-L. Hsu, A. R. Damodaran, L.-L. Li, A. K. Yadav, M. McCarter, L. W. Martin, R. Ramesh, and S. V. Kalinin, Quantification of flexoelectricity in $\mathrm{PbTiO_3/SrTiO_3}$ superlattice polar vortices using machine learning and phase-field modeling, Nat. Commun. **8**, 1468 (2017).

[46] Y. Nahas, S. Prokhorenko, L. Louis, Z. Gui, I. Kornev, and L. Bellaiche, Discovery of stable skyrmionic state in ferroelectric nanocomposites, Nat. Commun. **6**, 8542 (2015).

[47] R. Zhu, Z. Jiang, X. Zhang, X. Zhong, C. Tan, M. Liu, Y. Sun, X. Li, R. Qi, K. Qu, Z. Liu, M. Wu, M. Li, B. Huang, Z. Xu, J. Wang, K. Liu, P. Gao, J. Wang, J. Li *et al.*, Dynamics of polar skyrmion bubbles under electric fields, arXiv:2107.13390.

[48] J. Wang and T.-Y. Zhang, Effect of long-range elastic interactions on the toroidal moment of polarization in a ferroelectric nanoparticle, Appl. Phys. Lett. **88**, 182904 (2006).

[49] Q. Zhang, L. Xie, G. Liu, S. Prokhorenko, Y. Nahas, X. Pan, L. Bellaiche, A. Gruverman, and N. Valanoor, Nanoscale bubble domains and topological transitions in ultrathin ferroelectric films, Adv. Mater. **29**, 1702375 (2017).

[50] Z. Hong, A. R. Damodaran, F. Xue, S. L. Hsu, J. Britson, A. K. Yadav, C. T. Nelson, J. J. Wang, J. F. Scott, L. W. Martin, R. Ramesh, and L. Q. Chen, Stability of polar vortex lattice in ferroelectric superlattices, Nano Lett. **17**, 2246 (2017).

[51] G. Catalan, J. Seidel, R. Ramesh, and J. F. Scott, Domain wall nanoelectronics, Rev. Mod. Phys. **84**, 119 (2012).

[52] See Supplemental Material at http://link.aps.org/supplemental/10.1103/PhysRevB.105.224101 for (1) schematic of the bilayers and polar texture of a skyrmion bubble, (2) portrayal of gain density and negative permittivity of a skyrmion bubble, and (3) the variation of IP polarization distribution during tension and compression.

[53] J. J. P. Peters, G. Apachitei, R. Beanland, M. Alexe, and A. M. Sanchez, Polarization curling and flux closures in multiferroic tunnel junctions, Nat. Commun. **7**, 13484 (2016).

[54] K. Du, M. Zhang, C. Dai, Z. N. Zhou, Y. W. Xie, Z. H. Ren, H. Tian, L. Q. Chen, G. Van Tendeloo, and Z. Zhang, Manipulating topological transformations of polar structures through real-time observation of the dynamic polarization evolution, Nat. Commun. **10**, 4864 (2019).

[55] J. Wang, S.-Q. Shi, L.-Q. Chen, Y. Li, and T.-Y. Zhang, Phase-field simulations of ferroelectric/ferroelastic polarization switching, Acta Mater. **52**, 749 (2004).

[56] F.-H. Gong, Y.-L. Tang, Y.-L. Zhu, H. Zhang, Y.-J. Wang, Y.-T. Chen, Y.-P. Feng, M.-J. Zou, B. Wu, W.-R. Geng, Y. Cao, and X.-L. Ma, Atomic mapping of periodic dipole waves in ferroelectric oxide, Sci. Adv. **7**, eabg5503 (2021).

[57] J. Gao, F. Li, Z. Xu, C. Zhang, Y. Liu, G. Liu, T. Zhang, and H. He, Ferroelectric phase transitions and electromechanical properties of barium titanate and lead titanate crystals under uniaxial and shear stresses: A thermodynamic analysis, J. Phys. D: Appl. Phys. **46**, 215304 (2013).

[58] D. G. Schlom, L.-Q. Chen, C.-B. Eom, K. M. Rabe, S. K. Streiffer, and J.-M. Triscone, Strain tuning of ferroelectric thin films, Annu. Rev. Mater. Res. **37**, 589 (2007).

[59] V. G. Koukhar, N. A. Pertsev, and R. Waser, Thermodynamic theory of epitaxial ferroelectric thin films with dense domain structures, Phys. Rev. B **64**, 214103 (2001).

[60] Y. L. Li, S. Y. Hu, Z. K. Liu, and L. Q. Chen, Phase-field model of domain structures in ferroelectric thin films, Appl. Phys. Lett. **78**, 3878 (2001).